NASA/TP-20260008568

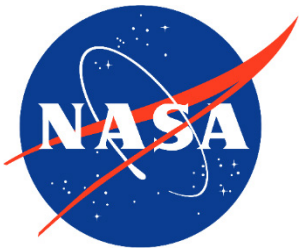

An Accurate and Computationally Efficient Heavy Ion Isotope Grid for HZETRN

Tony C. Slaba

NASA Langley Research Center, Hampton, Virginia

September 2026

NASA STI Program Report Series

Since its founding, NASA has been dedicated to the advancement of aeronautics and space science. The NASA scientific and technical information (STI) program plays a key part in helping NASA maintain this important role.

The NASA STI program operates under the auspices of the Agency Chief Information Officer. It collects, organizes, provides for archiving, and disseminates NASA's STI. The NASA STI program provides access to the NTRS Registered and its public interface, the NASA Technical Reports Server, thus providing one of the largest collections of aeronautical and space science STI in the world. Results are published in both non-NASA channels and by NASA in the NASA STI Report Series, which includes the following report types:

- TECHNICAL PUBLICATION. Reports of completed research or a major significant phase of research that present the results of NASA Programs and include extensive data or theoretical analysis. Includes compilations of significant scientific and technical data and information deemed to be of continuing reference value. NASA counterpart of peer-reviewed formal professional papers but has less stringent limitations on manuscript length and extent of graphic presentations.

- TECHNICAL MEMORANDUM. Scientific and technical findings that are preliminary or of specialized interest, e.g., quick release reports, working papers, and bibliographies that contain minimal annotation. Does not contain extensive analysis.

- CONTRACTOR REPORT. Scientific and technical findings by NASA-sponsored contractors and grantees.

- CONFERENCE PUBLICATION. Collected papers from scientific and technical conferences, symposia, seminars, or other meetings sponsored or co-sponsored by NASA.

- SPECIAL PUBLICATION. Scientific, technical, or historical information from NASA programs, projects, and missions, often concerned with subjects having substantial public interest.

- TECHNICAL TRANSLATION. English-language translations of foreign scientific and technical material pertinent to NASA's mission.

Specialized services also include organizing and publishing research results, distributing specialized research announcements and feeds, providing information desk and personal search support, and enabling data exchange services.

For more information about the NASA STI program, see the following:

- Access the NASA STI program home page at http://www.sti.nasa.gov

.

NASA/TP-20260008568

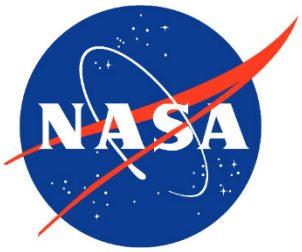

An Accurate and Computationally Efficient Heavy Ion Isotope Grid for HZETRN

Tony C. Slaba

NASA Langley Research Center, Hampton, Virginia

National Aeronautics and
Space Administration

Langley Research Center
Hampton, Virginia 23681-2199

September 2026

The use of trademarks or names of manufacturers in this report is for accurate reporting and does not constitute an official endorsement, either expressed or implied, of such products or manufacturers by the National Aeronautics and Space Administration.

Available from:

NASA STI Program / Mail Stop 050
NASA Langley Research Center
Hampton, VA 23681-2199

Contents

1. Abstract **1**
2. Introduction **1**
3. Methods **3**
4. Results and Discussion **6**
5. Summary and Conclusions **8**
6. Acknowledgements **8**
7. References **8**
Appendix **10**

Figures

1. Half-lives, $t_{1/2}$ (sec), of known isotopes for elements between Z = 3 – 28. The data were extracted from the IAEA LiveChart application (https://nds.iaea.org/relnsd/vcharthtml/VChartHTML.html). 4

2. Mass histogram, H_Z (A), behind 20 g/cm^2 aluminum shielding during solar minimum (Φ = 450 MV). HZETRN2020 results were calculated using an isotope grid with 601 heavy ions. The Geant4 and PHITS Monte Carlo simulations included all heavy ions available in the respective codes. 5

3. Sorted mass histogram for S (Z = 16) behind 20 g/cm^2 aluminum shielding during solar minimum (Φ = 450 MV) calculated by HZETRN2020. 5

4. Integral elemental flux, F_Z (pfu), as a function of charge, Z, behind 20 g/cm^2 aluminum shielding during solar minimum (Φ = 450 MV) from Geant4 (red) and PHITS (blue) simulations, and HZETRN2020 (black/gray). The HZETRN2020 results were calculated with various heavy ion isotope grids, as indicated.....7

5. Integral mass flux, F_A (pfu) behind 20 g/cm^2 aluminum shielding during solar minimum (Φ = 450 MV) from Monte Carlo simulations (x-axis) and HZETRN2020 (y-axis). The HZETRN2020 results were calculated with various heavy ion isotope grids, as indicated. The average absolute percent difference between HZETRN2020 and Geant4/PHITS is given in red/blue text, respectively. For comparative purposes, the PHITS results differed from Geant4 by ~14%. 7

Tables

1. Summary of p values, heavy ion grid sizes, calculated exposure quantities, and run times. Calculations were performed for 20 g/cm^2 aluminum shielding protecting a 35 year old female never smoker on a 1 year mission during solar minimum (Φ = 450 MV). Dose equivalent, NASA effective dose, and REID were calculated with the 2025 NASA space cancer risk model [Slaba et al. 2026]. Dose and dose equivalent were calculated behind shielding without any human phantom or tissue shielding, and the dose equivalent utilizes the solid cancer quality factor. 6

1. Abstract

NASA has developed a deterministic radiation transport code, HZETRN, to enable accurate and efficient radiation exposure estimates for humans and sensitive electronics. The code tracks primary particles comprising the ambient radiation field impinging on the spacecraft structure and shielding as well as any secondary particles produced as a result of physical interactions. The most recent version, HZETRN2020, includes gammas, leptons, muons, pions, nucleons, deuterons, tritons, helions, alphas, and a list of 53 heavier ions (heavy ion grid) spanning elements from Li to Ni. The 53-ion grid provides sufficient accuracy for total integrated quantities of interest to space radiation protection such as absorbed dose, dose equivalent, NASA effective dose, and cancer risk metrics. However, if the elemental flux spectra underlying these quantities are examined as a function of mass, notable errors can be found and attributed to inadequate isotopic resolution within the 53-ion grid. In this work, a state-of-the-art galactic cosmic ray (GCR) propagation model, GALPROP, is used to assess solar modulation and energy-dependent isotopic contributions to elemental GCR fluxes calculated with the Badhwar-O'Neill 2020 GCR model. The isotope dependent GCR model is used as input to HZETRN2020, and calculations are performed over a range of shielding and solar cycle conditions with heavy ion grids including as many as 601 particles. Convergence testing is used to identify a suitably accurate heavy ion grid that retains computational efficiency within HZETRN2020. A grid with 77 heavy ions is subsequently defined and recommended for use in HZETRN2020 and future versions.

2. Introduction

Galactic cosmic rays (GCR) represent the primary radiation hazard for long duration human spaceflight missions beyond low Earth orbit. The GCR environment constitutes a complex mixed field of energetic ions capable of penetrating through spacecraft shielding and inducing biological damage within radiosensitive tissue sites. These ions also suffer nuclear collisions as they pass through mass shielding in which secondary radiation may be produced, including energetic gammas, leptons, mesons, nucleons, and other charged particles.

An accurate characterization of the complex radiation field found within radiosensitive tissues of humans behind shielding in space is required to facilitate reliable health risk projections and ensure crew safety. NASA has therefore developed the deterministic space radiation transport code, HZETRN, to enable such characterizations to be performed in a highly efficient manner in support of preflight engineering design optimization and postflight exposure assessment. The most recent version of HZETRN, referred to herein as HZETRN2020 [Slaba et al. 2020], includes both one-dimensional and three-dimensional transport physics options that can be used to analyze either simple geometries (slabs, spheres, boxes, etc.) or highly complex human rated vehicle and habitat geometries developed in computer-aided design software. Specific methods have been developed and integrated into the code to treat neutron diffusion [Wilson et al. 2021], low energy proton recoils in hydrogenous materials, negative pion capture, and surface muons [Slaba et al. 2020]. Nuclear interactions are described by an integrated set of models to cover the broad range of projectiles, fragments, energies, and targets relevant to space radiation protection [Werneth et al. 2025].

Due to the deterministic formulation, all versions of HZETRN require a prescribed list of particles to include in transport procedures. HZETRN2020 includes γ, $e^{\pm}$, $\mu^{\pm}$, $\pi^{\pm}$, n, p, ^{2}H, ^{3}H, ^{3}He, ^{4}He, and a list of heavier ions with charges ranging from $Z = 3$ to $Z = 28$, hereafter referred to as the heavy ion isotope grid. The 2005 version of HZETRN [Wilson et al. 2006] included an isotope grid with 53 heavy ions, which can be found in the Appendix. The 53 heavy ion isotope grid has been carried into subsequent versions of HZETRN, including HZETRN2020 and the OLTARIS website (available at https://oltaris.nasa.gov).

It will be shown that the 53-ion isotope grid provides sufficient accuracy for quantities of interest to space radiation protection such as total absorbed dose, dose equivalent, NASA effective dose, and risk of exposure induced death (REID). These quantities are all primarily influenced by the underlying elemental (charge) distribution and are less sensitive to the isotopic (mass) composition. Nevertheless, if such quantities are examined as a function of ion mass, the 53-ion grid may lack sufficient fidelity to accurately describe the isotopic nature of either the primary GCR field or the induced radiation field found behind shielding.

Cucinotta et al. [2006] previously examined the isotopic dependence of both the primary GCR field and the induced field behind shielding. In their work, a collection of measurements [Hesse et al. 1991; Lukasiak et al. 1993, 1995; Webber et al. 1985, 1990; Wiedenback and Greiner 1981; Wiedenback 1985] taken near solar maximum were analyzed to produce energy-independent isotopic fractions for GCR elements with $Z = 3 – 26$ (absent $Z = 9, 11, 15, 19, 21$). An empirical formula was introduced to represent the influence of solar modulation on the GCR isotopic fractions. This initial and simplified isotopic fraction model was coupled to an early version of the Badhwar-O'Neill (BON) GCR model [Badhwar and O'Neill 1992] via the equation

$$f(E,A,Z,\Phi) = f_{\mathrm{BON}}(E,Z,\Phi)\,\alpha(A,Z,\Phi)\,, \tag{1}$$

where $f_{\mathrm{BON}}(E,Z,\Phi)$ is the elemental GCR flux calculated from the BON model, and $\alpha(A,Z,\Phi)$ (unitless) is the energy-independent isotopic fraction. The variables E, A, and Z are the particle kinetic energy (MeV/n), mass, and charge, respectively. The symbol Φ (MV) is the solar modulation parameter. The fractions are normalized to satisfy

$$\sum_{A} \alpha(A,Z,\Phi) = 1\,, \tag{2}$$

so that the total elemental fluxes provided by the BON model are preserved within $f(E,A,Z,\Phi)$.

Cucinotta et al. [2006] used this initial isotope-dependent GCR model as input to an earlier version of HZETRN along with an expanded isotope grid including 163 heavy ions. Calculations were performed for solar minimum and solar maximum behind 5 g/cm^2 and 20 g/cm^2 aluminum shielding. Mass fluence distributions calculated with the 163-ion grid differed substantially from the simpler 53-ion grid. The differences were expected though, since the expanded grid included many isotopes that were entirely absent from the simpler grid. It was argued that the more expansive 163-ion grid is easily handled by available computational resources and should therefore be used. However, differences introduced by these isotope grids into total integrated quantities relevant to space radiation protection were not reported. No run-time comparisons were provided to allow computational cost to be balanced against any changes in accuracy.

Key modeling advancements have occurred in the past 20 years providing improved predictions of the isotopic nature of the ambient GCR environment and the mass distribution of secondaries produced from nuclear fragmentation events in bulk shielding. First, GALPROP (https://galprop.stanford.edu) [Vladimirov et al. 2011] is a state-of-the-art computational model developed to study the propagation of relativistic cosmic rays through the galaxy. It is widely used in astrophysical research applications, but the specific capability of interest here is the treatment of nuclear fragmentation of cosmic ray source ions as they traverse the heliosphere. The model is used in this work to expand the isotopic fraction, α, appearing in equation (1) to include energy dependence and provide a more thorough description of mass-dependence in the GCR environment at all phases of the solar cycle. Second, the Relativistic Abrasion Ablation Deexcitation FRaGmentation (RAADFRG) model [Werneth et al. 2021] has been developed to describe heavy ion nuclear interactions within HZETRN2020. The RAADFRG model includes relativistic kinematics and accounts for nuclear structure effects that manifest even-odd behavior observed in ground-based experimental data. It has been extensively validated and exhibits a high degree of accuracy over the range of ions, energies, and targets relevant to space radiation shielding studies [Werneth et al. 2021].

In this work, these modeling advancements are utilized to support an updated analysis of the isotopic nature of the GCR environment and the induced radiation field behind shielding. The primary motivation of this work is to define an optimal isotope grid for use in HZETRN2020 that accurately describes the charge and mass dependence of the GCR field encountered by astronauts behind shielding while maintaining computational efficiency.

The energy-independent isotopic fraction, α, appearing in equation (1) is replaced with a database generated by the GALPROP model [Vladimirov et al. 2011]. The database encompasses isotopes for all elements with $Z = 1 - 28$, energies ranging from 10^1 MeV/n to 10^6 MeV/n, and solar modulation conditions from deep solar minimum to extreme solar maximum. The elemental GCR flux is computed with an updated version of the BON model [Slaba and Whitman 2020], referred to as BON2020, which has been extensively and successfully validated [Slaba and Whitman 2020, Liu et al. 2024]. The GALPROP model results are combined with BON2020 to produce an isotope-dependent GCR model.

Isotopic GCR spectra are used as input to HZETRN2020, and transport calculations are performed through various levels of shielding up to 100 g/cm^2 using a high-fidelity heavy ion grid with over 600 particles. Utilizing these results, a method is developed that systematically defines smaller isotope grids and allows changes in accuracy and computational cost to be quantified simultaneously. HZETRN2020 results obtained with the various isotope grids are compared to Monte Carlo simulations to provide a level of verification and context for nuclear fragmentation model uncertainties.

3. Methods

Isotopic GCR model

The isotope-dependent GCR model is expressed similarly to equation (1) as

$$f(E,A,Z,\Phi) = f_{\mathrm{BON\,2020}}(E,Z,\Phi)\alpha_{\mathrm{GALPROP}}(E,A,Z,\Phi_G)\,, \tag{3}$$

where $f_{\mathrm{BON2020}}(E,Z,\Phi)$ (particles/(cm^2-MeV/n-day) is the elemental GCR flux calculated from the BON2020 model which has been described in detail elsewhere [Slaba and Whitman 2020]. The symbol $\alpha_{\mathrm{GALPROP}}$ denotes the isotopic fraction for each element Z, dependent on both solar modulation, Φ_G, and kinetic energy. The GALPROP isotopic fractions are normalized similarly to equation (2) as

$$\sum_A \alpha_{\mathrm{GALPROP}}(E,A,Z,\Phi_G) = 1\,, \tag{4}$$

to ensure the elemental fluxes from BON2020 are preserved. Further details for $\alpha_{\mathrm{GALPROP}}$ and Φ_G will be provided below. The primary difference between equations (1) and (3) rests in the isotopic fraction, which is now based on the energy-dependent GALPROP model. For this work, the GALPROP ver. 54 WebRun tool [Vladimirov et al. 2011] was utilized for all calculations.

To facilitate practical integration of the GALPROP WebRun results within equation (3), a database interpolation approach was developed. First, GALPROP was evaluated using a default configuration file calibrated to agree with measurements from the Advanced Composition Explorer (ACE) [Stone et al. 1998]. Next, isotopic fractions were derived from the simulation results for a range of solar modulation parameters (200, 400, 800, 1200, 1600, 2000, 2500, 3000 MV) and kinetic energies (10, 50, 10^2, 2×10^2, 5×10^2, 10^3, 2×10^3, 5×10^3, 10^4, 2×10^4, 5×10^4, 10^5, 10^6 MeV/n). The derived isotopic fractions for elements with Z = 1 – 28 for all solar modulation and kinetic energy combinations were assembled in a database. Interpolation methods are then utilized to allow $\alpha_{\mathrm{GALPROP}}$ to be computed as needed in (3).

A final detail needing to be addressed is the distinction between Φ and Φ_G. Both symbols represent solar modulation parameters, but their magnitudes are model dependent. To determine the precise relationship between the two parameters, elemental GCR fluxes from GALPROP WebRun for a given Φ_G were compared to BON2020 calculations over a broad range of Φ values. The Φ value providing the best agreement between the BON2020 and GALPROP WebRun results was then associated with Φ_G. The process was repeated over several Φ_G values, yielding the empirical relationship

$$\Phi_G = 1.27\Phi - 189.01\,. \tag{5}$$

Thus, equation (5) ensures the notions of solar modulation used to calculate the BON2020 elemental flux spectra and GALPROP isotopic ratios are aligned within equation (3).

Radiation Transport and Isotope Grid Definitions

The HZETRN2020 transport code [Slaba et al. 2020] and RAADFRG heavy ion nuclear fragmentation model [Werneth et al. 2021] are used to propagate isotopic GCR spectra through various shielding configurations. Further details of these models can be obtained from the references provided. To facilitate convergence testing and enable isotope grid fidelity to be balanced against accuracy and computational cost, a grid with 601 heavy ions was generated. The 601-ion grid allows mass dependence in GALPROP and RAADFRG to be fully retained throughout transport calculations. The grid was extracted from the International Atomic Energy Agency (IAEA) LiveChart application (https://nds.iaea.org/relnsd/vcharthtml/VChartHTML.html) which provides half-lives, $t_{1/2}$ (sec), of all known isotopes for the elements of interest in this work (Z = 3 – 28) and is plotted in Figure 1.

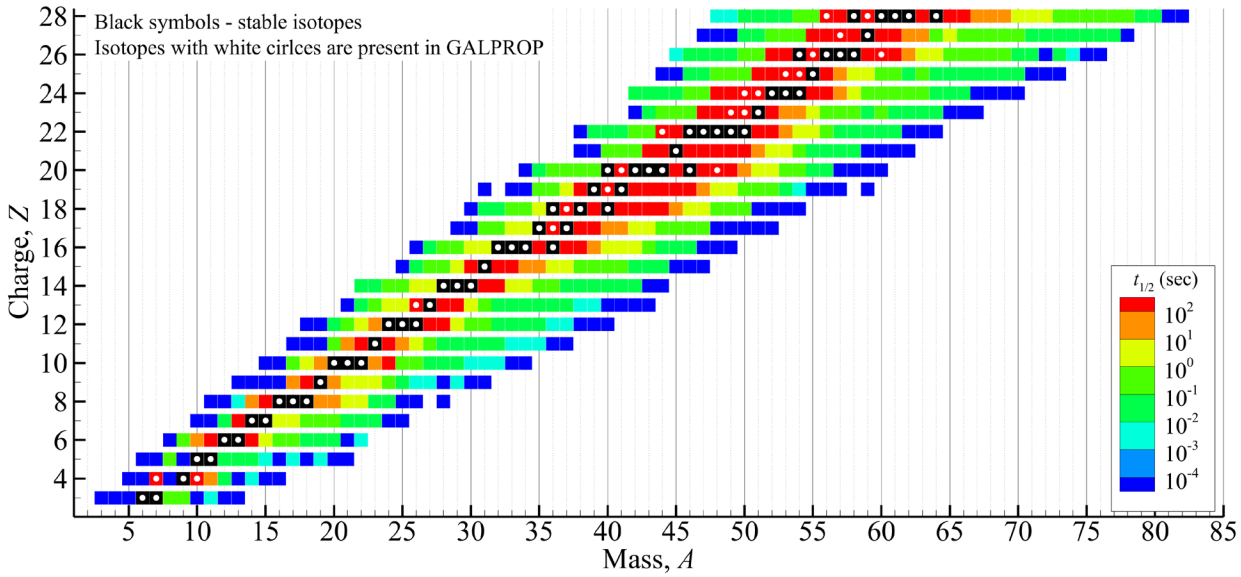

Figure 1. Half-lives, $t_{1/2}$ (sec), of known isotopes for elements between $Z = 3 – 28$. The data were extracted from the IAEA LiveChart application (https://nds.iaea.org/relnsd/vcharthtml/VChartHTML.html).

Transport calculations were performed with the 601-ion grid over a range of aluminum shielding thicknesses up to 100 g/cm^2 and solar modulation parameters between $\Phi = 450$ (solar minimum) and $\Phi = 1200$ MV (solar maximum). Charge-dependent mass histograms were derived from the transport calculations according to

$$H_Z(A) = \frac{F(A,Z)}{F_Z}, \tag{6}$$

$$F(A,Z) = \int \phi(E,A,Z)\,dE, \qquad F_Z = \sum_A F(A,Z), \qquad F_A = \sum_Z F(A,Z), \tag{7}$$

where $\phi(E,A,Z)$ (particles/(cm^2-MeV/n-day)) is the flux of particles with kinetic energy E (MeV/n), mass A, and charge Z calculated for a prescribed aluminum shielding thickness and solar modulation level. The quantities $F(A,Z)$, F_Z, and F_A have the units of particles/(cm^2-day), which is denoted hereafter as the particle flux unit (pfu). Equation (6) is defined such that

$$\sum_A H_Z(A) = 1. \tag{8}$$

Sample histograms are provided in Figure 2 for 20 g/cm^2 aluminum shielding during solar minimum conditions ($\Phi = 450$ MV). Also shown in the figure for comparative purposes are results from the Geant4 version 10.5 [Allison et al. 2016] and PHITS version 3.33 [Sato et al. 2024] Monte Carlo simulation codes. Mass histograms from the three transport codes utilizing distinct heavy ion fragmentation models are qualitatively similar. The peaks for each element correspond to primary GCR isotopes. Transport processes for these particles are dominated by atomic energy loss and total nuclear reaction cross sections, for which uncertainties are relatively small. Results from the various codes for these particles are therefore in excellent agreement. Isotopes above or below the primary GCR particle peaks correspond to secondary particles produced in nuclear fragmentation events. Visible differences can be seen in the transport code results for these secondary particles, attributable to larger uncertainties in nuclear fragmentation models traceable to sparse ground-based experimental data [Norbury and Miller 2012, Norbury et al. 2012]. Nevertheless, results from the three codes can be considered highly similar over a broad range of elements and isotopes. Though not shown, the same conclusions were reached from analyzing results for other shielding thicknesses and solar modulation levels.

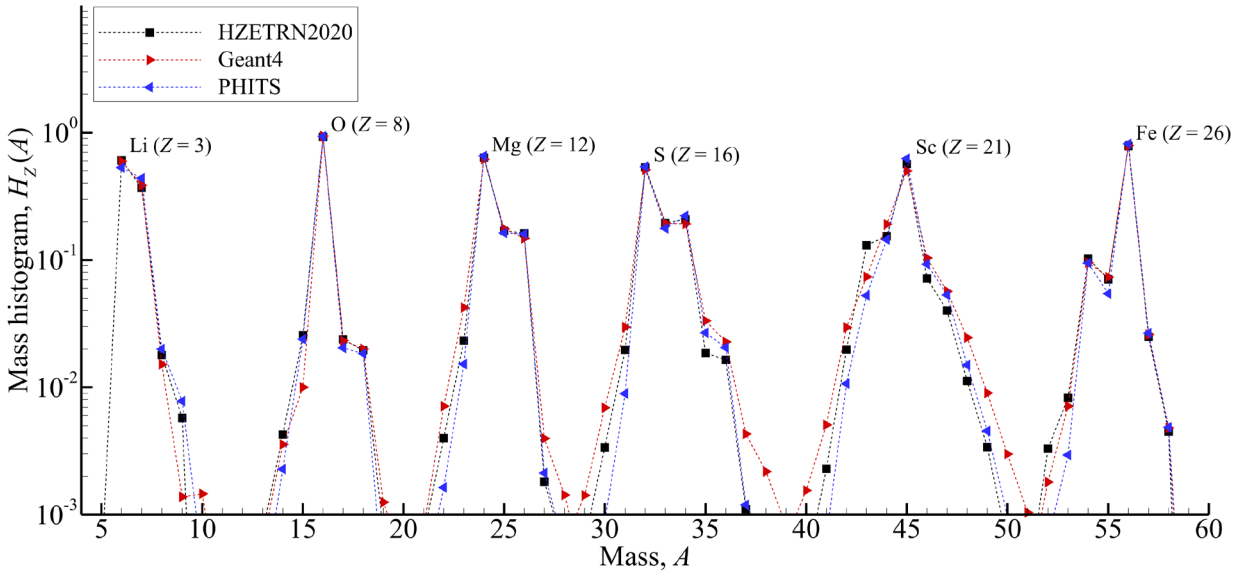

Figure 2. Mass histogram, $H_Z(A)$, behind 20 g/cm^2 aluminum shielding during solar minimum (Φ = 450 MV). HZETRN2020 results were calculated using an isotope grid with 601 heavy ions. The Geant4 and PHITS Monte Carlo simulations included all heavy ions available in the respective codes.

The charge-dependent mass histograms, $H_Z(A)$, calculated for aluminum shielding thicknesses up to 100 g/cm^2 and solar modulation parameters between Φ = 450 – 1200 MV are used to define isotope grids for convergence testing. For each scenario and element, all isotopes were sorted according to their histogram weight. A precision level, p, is then introduced to provide a systematic basis for isotope selection. An example sorted mass histogram for S (Z = 16) is shown in Figure 3, along with ranges of isotopes that would be selected for p values ranging from 0.9 (i.e., 90% of the mass histogram) to 0.999 (i.e., 99.9% of the mass histogram).

The p values shown in Figure 3 were used in this work to drive isotope grid selection. The sorted mass histogram analysis was conducted for each element in the range Z = 3 – 28 over the set of transport calculations encompassing aluminum shield thickness up to 100 g/cm^2 and solar modulation parameters from Φ = 450 MV to Φ = 1200 MV. Selected isotopes for each element therefore satisfy the precision level, p, over a broad range of shielding thicknesses and solar modulation levels of interest to space radiation protection.

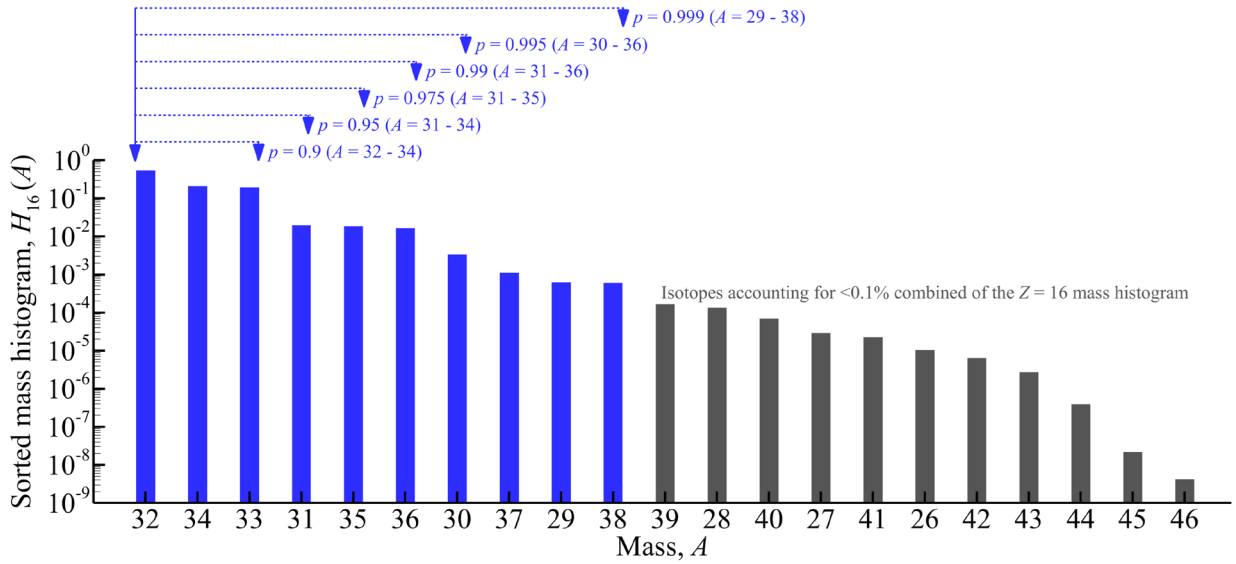

Figure 3. Sorted mass histogram for S (Z = 16) behind 20 g/cm^2 aluminum shielding during solar minimum (Φ = 450 MV) calculated by HZETRN2020.

4. Results and Discussion

Isotope grid sizes generated by p values ranging from 0.9 to 0.999 are given in Table 1. Various exposure quantities of interest calculated with the isotope grids within HZETRN2020 are also provided in the table. The dose and dose equivalent values are calculated behind shielding without any human phantom or tissue shielding. NASA effective dose and REID values include additional transport through a detailed human phantom [Slaba et al. 2010, 2026]. The run time listed in the last column represents the total time required to complete the entire set of calculations. This includes evaluation of the GCR environment and transport through materials (aluminum shielding and/or tissue) along with calculation of dose, dose equivalent, NASA effective dose, and REID. Results will be given for solar minimum conditions (Φ = 450 MV) and 20 g/cm^2 aluminum shielding. Other solar modulation and shielding levels were examined as well and yielded qualitatively similar results and conclusions.

The integrated response quantities in Table 1 are barely affected by the isotope grid size. Across all isotope grids considered, the dose varied by less than 0.1%; the remaining quantities all varied by less than 0.4%. This is an expected result, since the exposure quantities are mainly sensitive to the charge (Z) distribution and depend weakly on the isotopic mass (A) composition underlying each charge.

Integral elemental fluxes, F_Z, are shown in Figure 4. It can again be seen that results from all three transport codes, utilizing distinct nuclear fragmentation models, are in excellent agreement. The HZETRN2020 results also appear largely insensitive to the fidelity of the isotope grid. This is also expected and consistent with the results in Table 1, since all charges from Z = 3 to Z = 28 are included in each of the isotope grids.

Table 1. Summary of p values, heavy ion grid sizes, calculated exposure quantities, and run times. Calculations were performed for 20 g/cm^2 aluminum shielding protecting a 35 year old female never smoker on a 1 year mission during solar minimum (Φ = 450 MV). Dose equivalent, NASA effective dose, and REID were calculated with the 2025 NASA space cancer risk model [Slaba et al. 2026]. Dose and dose equivalent were calculated behind shielding without any human phantom or tissue shielding, and the dose equivalent utilizes the solid cancer quality factor.

p	Heavy ion grid size	Dose (mGy/year)	Dose equivalent (mGy/year)	NASA effective dose (mSv/year)	REID (%)	Run time (sec)
	53	166.8	510.8	353.7	1.585	22.5
0.9	66	166.8	511.4	354.1	1.587	27.0
0.95	77	166.8	511.4	354.1	1.587	30.9
0.975	92	166.9	511.4	354.1	1.587	35.7
0.99	112	166.9	512.1	354.8	1.590	45.1
0.995	131	166.9	512.4	355.1	1.592	54.9
0.999	168	166.9	512.5	355.1	1.592	76.5
	601	166.9	512.5	355.1	1.592	474.1

Integral mass fluxes, F_A, from Geant4, PHITS, and HZETRN2020 are shown in Figure 5. The average absolute percent difference between HZETRN2020 and Geant4/PHITS is given in red/blue text, respectively. It can be seen in the top left corner of Figure 5 that results from HZETRN2020 with the 601-ion grid were within 16% of Geant4 and 13% of PHITS. These relative differences are quite comparable to the relative difference between PHITS and Geant4 of ~14% and are related to uncertainty introduced by heavy ion nuclear fragmentation models. Further ground-based experimental data would be needed to reduce this uncertainty, but it is concluded that the heavy ion fragmentation models used in the three transport codes agree reasonably well with each other in this application.

The grids with >100 ions (top row of Figure 5) yield integral mass fluxes within 14% - 17% of the Monte Carlo simulation results, almost identical to the accuracy provided by the 601-ion grid. No clear advantage in accuracy is achieved by using more than 112 ions. Additional isotopic fidelity associated with the 131-ion and 168-ion grids is therefore superfluous especially given the associated computational cost, as shown in Table 1. It can also be seen in Figure 5 that relative differences between HZETRN2020 and the Monte Carlo simulation results systematically increase as isotope grid fidelity is reduced. In particular, despite the fact that the 53-ion grid used in HZETRN2020 is sufficiently accurate for total integrated quantities (Table 1) and integral elemental fluxes (Figure 4), substantial errors >50% in the integral mass fluxes are observed.

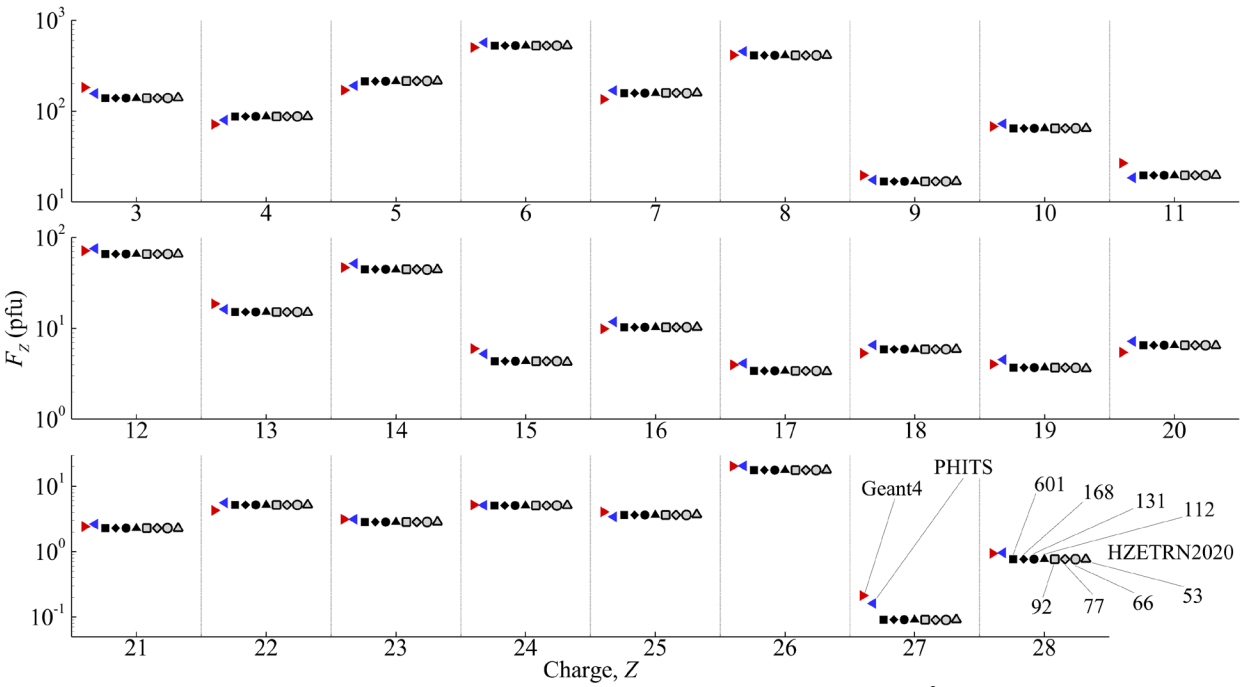

Figure 4. Integral elemental flux, F_Z (pfu), as a function of charge, Z, behind 20 g/cm^2 aluminum shielding during solar minimum (Φ = 450 MV) from Geant4 (red) and PHITS (blue) simulations, and HZETRN2020 (black/gray). The HZETRN2020 results were calculated with various heavy ion isotope grids, as indicated.

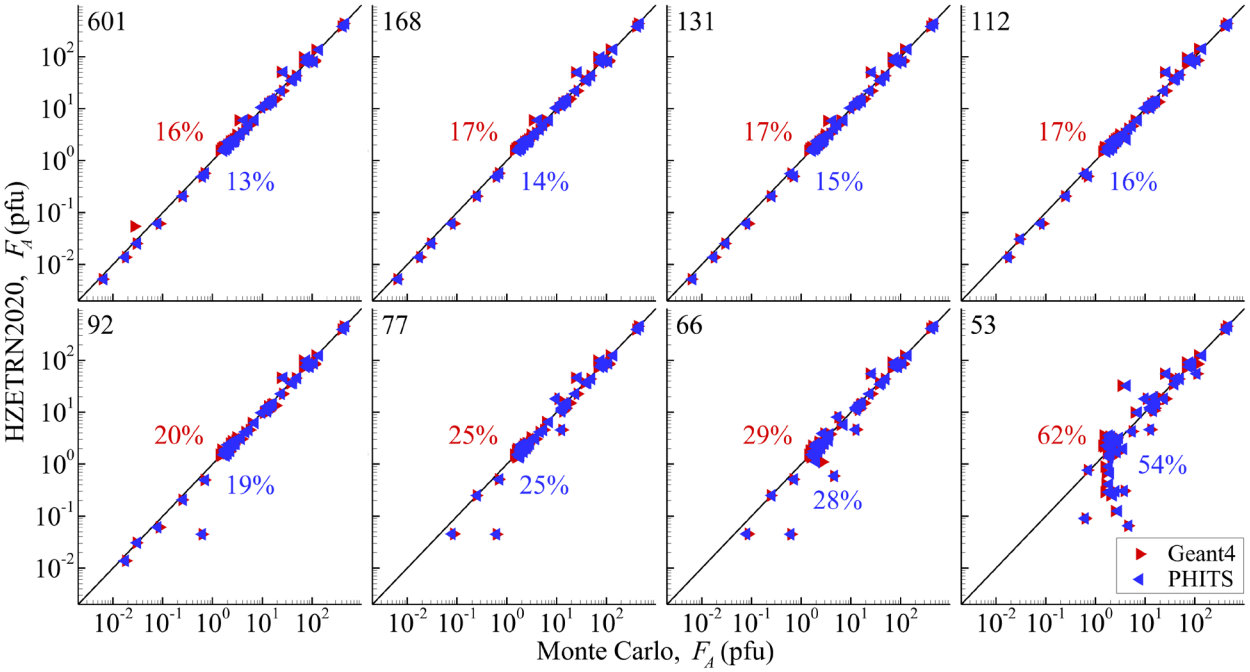

Figure 5. Integral mass flux, F_A (pfu) behind 20 g/cm^2 aluminum shielding during solar minimum (Φ = 450 MV) from Monte Carlo simulations (x-axis) and HZETRN2020 (y-axis). The HZETRN2020 results were calculated with various heavy ion isotope grids, as indicated. The average absolute percent difference between HZETRN2020 and Geant4/PHITS is given in red/blue text, respectively. For comparative purposes, the PHITS results differed from Geant4 by ~14%.

To balance overall accuracy and computational cost, the 77-ion isotope grid (documented in the Appendix) is identified as an improved replacement for the 53-ion grid. It has already been demonstrated that the 77-ion grid provides sufficient accuracy for the quantities of interest to space radiation protection (Table 1) and the elemental fluxes underlying such quantities (Figure 4). The 77-ion grid yields an integral mass flux error of approximately 25% (Figure 5) which is more than 2x smaller than the error associated with the 53-ion grid and comparable to errors attributable to much larger grids. The notable increase in accuracy comes at a very modest increase in computational cost that is considered acceptable for general use within HZETRN2020.

5. Summary and Conclusions

In this work, heavy ion grid fidelity required to ensure accuracy in mass fluxes while retaining computational efficiency within HZETRN2020 was studied. The GALPROP model was evaluated to provide solar cycle and energy dependent isotopic fractions for each element from H to Ni. These isotopic fractions were integrated with the BON2020 model to allow isotope-dependent GCR fluxes to be calculated for each element. Isotopic GCR spectra were used as input to HZETRN2020, which utilizes the RAADFRG heavy ion nuclear fragmentation model, to evaluate various exposure quantities of interest over a wide range of shielding and solar cycle conditions. The calculations were additionally performed using multiple different heavy ion grids including anywhere from 53 to 601 particles.

Analysis of these results confirmed that isotope grid fidelity has a negligible effect on total integrated quantities of interest to space radiation protection, such as absorbed dose, dose equivalent, NASA effective dose, and REID. If the particle fluxes underlying these quantities are examined as a function of ion mass, notable errors were observed in the results based on the 53-ion grid. It was found that grids with 112 or more ions provide little benefit in accuracy but greatly increase computational cost. A 77-ion grid was identified that provides reasonable accuracy for mass fluxes while retaining computational efficiency and is recommended for future use in HZETRN2020.

6. Acknowledgements

This work was supported by the NASA Mars Campaign Office (MCO) HZETRN Physics Development Project.

7. References

Allison, J., et al., Recent developments in Geant4. *Nuc. Instr. Meth. A* **835**: 186-225; 2016.

Badhwar, G.D., O'Neill, P.M., An improved model of GCR for space exploration missions. *Nucl. Tracks Radiat. Meas.* **20**: 403-410; 1992.

Cucinotta, F.A., Wilson, J.W., Saganti, P., Hu, X., Kim, M.Y., Cleghorn, T., Zeitlin, C., Tripathi, R.K., Isotopic dependence of GCR fluence behind shielding. *Rad. Mes.* **41**: 1235-1249; 2006.

Hesse, A., et al., The isotopic composition of silicon and iron in the cosmic radiation as measured by the ALICE experiment. 22nd International Conference, The Dublin Institute for Advanced Studies, Dublin, 596-599; 1991.

Liu, W., Guo, J., Wang, Y., Slaba ,T.C., A comprehensive comparison of various galactic cosmic-ray models to the state-of-the-art particle and radiation measurements. *Astrophys. J. Suppl.* **271**: 29; 2024.

Lukasiak, A., Ferrando, P., McDonald, F.B., Webber, W.R., Cosmic ray composition of $6<Z<8$ nuclei in the energy range 50-150 MeV/n by the Voyager spacecraft during the solar minimum and maximum periods. 23rd International Cosmic Ray Conference, 539–542; 1993.

Lukasiak, A., McDonald, F.B., Webber, W.R., Ferrando, P., Voyager measurements of the isotopic composition of Sc, Ti, V, Cr, Mn, and Fe nuclei. 24th International Conference Ray Conference, 576-579; 1995.

Norbury, J.W. and Miller, J., Review of nuclear physics experimental data for space radiation. *Health Phys.* **103**, 640-642; 2012.

Norbury, J.W., Miller, J. Adamczyk, A.M., Heilbronn, L.H., Townsend, L.W., Blattnig, S.R., Norman, R.B., Guetersloh, S.B., Zeitlin, C.J., Nuclear data for space radiation. *Rad. Meas.* **47**: 315-363; 2012.

Sato, T., Iwamoto, Y., Hashimoto, S., Ogawa, T., Furuta, T., Abe, S., Kai, T., Matsuya, Y., Matsuda, N., Hirata, Y., Sekikawa, T., Yao, L., Tsai, P.E., Ratliff, H.N., Iwase, H., Sakaki, Y., Sugihara, K., Shigyo, N., Sihver, L., Niita, K., Recent improvements of the particle and heavy ion transport code system - PHITS version 3.33. *J. Nucl. Sci. Technol.* **61**: 127-135; 2024.

Slaba, T.C., Qualls, G.D., Clowdsley, M.S., Blattnig, S.R., Walker, S.A., Simonsen, L.C., Utilization of CAM, CAF, MAX, and FAX for space radiation analyses using HZETRN. *Adv. Space Res.* **45**: 866-883; 2010.

Slaba, T.C. and Whitman, K., The Badhwar-O'Neill 2020 model. *Space Weather* **18**: e2020SW002456; 2020.

Slaba, T.C., Wilson, J.W., Werneth, C.M., Whitman, K., Updated deterministic radiation transport for future deep space missions. *Life Sci. Space Res.* **27**: 6-18; 2020.

Slaba, T.C., Werneth, C.M., Poignant, F., Huff, J.L., NASA space cancer risk model 2025: multi-model ensemble quality factor. NASA TP 2026-0006857; 2026.

Stone, E.C., Frandsen, A.M., Mewaldt, R.A., Christian, E.R., Margolies, D., Ormes, J.F., Snow, F., The advanced composition explorer, *Space Sci. Rev.* **86**: 1-22; 1998.

Vladimirov, A.E., Digel, S.W., Johannesson, G., Michelson, P.F., Moskalenko, I.V., Nolan, P.L., Orlando, E., Porter, T.A., Strong, A.W., GALPROP WebRun: an internet-based service for calculating galactic cosmic ray propagation and associated photon emissions. *Comput. Phys. Commun.* **182**: 1156-1161; 2011.

Webber, W.R., Kish, J.C., Schrier, D.A., Cosmic ray isotope measurements with a new cerenkov total energy telescope. 19th International Cosmic Ray Conference, 88-95; 1985.

Webber, W.R., Southoul, A., Ferrando, P., Gupta, M., The source charge and isotropic abundances of cosmic rays with $Z = 9–16$: a study using new fragmentation cross-sections. *Astrophys. J.* **348**: 611-620; 1990.

Werneth, C.M., de Wet, W.C., Townsend, L.W., Maung, K.M., Norbury, J.W., Slaba, T.C., Norman, R.B., Blattnig, S.R., Ford, W.P., Relativistic abrasion-ablation de-excitation fragmentation (RAADFRG) model. *Nuc. Instr. Meth. B* **502**: 118-135; 2021.

Werneth, C.M., Norbury, J.W., Slaba, T.C., Review of Nuclear Cross Section Models in HZETRN2020, NASA TP-2025-0009529; 2025.

Wiedenback, M.E., Greiner, D.E., High-resolution observations of the isotopic composition of carbon and silicon in the galactic cosmic rays. *Astrophys. J.* **247**: L119–L122; 1981.

Wiedenback, M.E., The isotopic composition on cosmic ray chlorine. 19th International Cosmic Ray Conference, 84-87; 1985.

Wilson, J.W., Tripathi, R.K., Badavi, F.F., Cucinotta, F.A., Standardized radiation shield design method: 2005 HZETRN. SAE ICES 2006-18; 2006.

Wilson, J.W., Slaba, T.C., Werneth, C.M., Badavi, F.F., Reddell, B.D., Bahadori, A.A., Neutron diffusion correction in 3DHZETRN-V2: ENDF/B. NASA TP 2021-0020403; 2021

Appendix

Table A1. List of particles included in the 53 and 77 heavy ion isotope grids. Rows in bold text indicate elements with the same isotopes in both grids.

Element	Charge, Z	Isotope masses, A	
		53-ion grid	77-ion grid
Li	**3**	**6, 7**	**6, 7**
Be	4	8, 9	7, 9, 10
B	**5**	**10, 11**	**10, 11**
C	**6**	**12, 13**	**12, 13**
N	**7**	**14, 15**	**14, 15**
O	**8**	**16, 17**	**16, 17**
F	9	18, 19	18, 19, 20
Ne	**10**	**20, 21, 22**	**20, 21, 22**
Na	11	23	22, 23
Mg	**12**	**24, 25, 26**	**24, 25, 26**
Al	13	27	26, 27
Si	14	28	28, 29, 30
P	15	29	30, 31, 32
S	16	30, 31, 32	32, 33, 34
Cl	17	33, 35	35, 36, 37
Ar	18	34, 36, 38	36, 37, 38, 40
K	19	37, 39	39, 40, 41
Ca	20	40, 41, 42	40, 41, 42, 43, 44
Sc	21	43	43, 44, 45, 46
Ti	22	44, 45, 46, 47	45, 46, 47, 48, 49
V	23	48, 49	48, 49, 50, 51
Cr	24	50, 51, 52	50, 51, 52, 53
Mn	25	53, 54	53, 54, 55
Fe	26	55, 56	54, 55, 56
Co	27	57	57, 59
Ni	28	58	58, 60